Powder Technology 425 (2023) 118574

Contents lists available at ScienceDirect

Powder Technology

journal homepage: www.journals.elsevier.com/powder-technology

A discrete element analysis of the mechanical behaviour of a lithium-ion battery electrode active layer

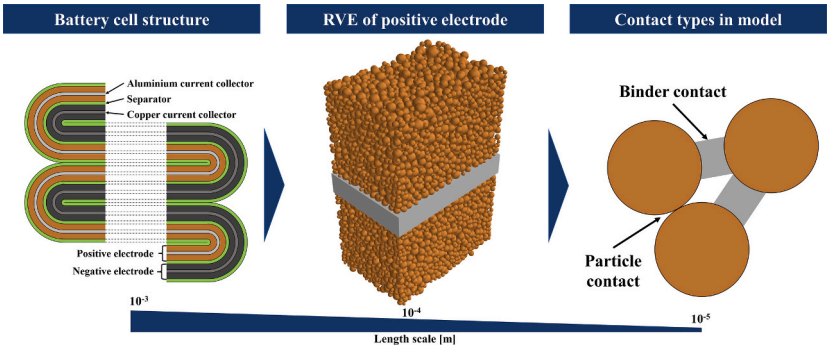
Axel Lundkvist [a], Per-Lennart Larsson [a], Erik Olsson [b,*]

[a] Department of Engineering Mechanics, Unit of Solid Mechanics, Royal Institute of Technology – KTH, Teknikringen 8, 100 44 Stockholm, Sweden
[b] Department of Engineering Sciences and Mathematics, Division of Solid Mechanics, Luleå University of Technology, Luleå, Sweden

HIGHLIGHTS

- A DEM model of positive electrode active layer of lithium-ion batteries has been developed.
- The model links the local contact between active particles to the macroscopic mechanical behaviour of the active layer.
- The model simulates the calendaring process followed by a virtual mechanical test.
- The model can capture the active layers different mechanical properties in compression and in tension.

GRAPHICAL ABSTRACT



ARTICLE INFO

Keywords:
Lithium-ion batteries
Discrete element method
Bonded contact model
Simulation
Calendering
Mechanical characterisation

ABSTRACT

Lithium-ion batteries experience charge capacity loss during their lifecycle caused by mechanical phenomena. In this study, a discrete element method (DEM) simulation model, to link the local mechanical behaviour in the positive electrode active layer to its global mechanical properties, was developed. DEM is a suitable method to use as the electrode active layer has a granular structure and the model includes contact formulations for the active particles and the binder domain. Simulations of the calendering process and the measurement of the active layer's global mechanical properties is possible with the framework. The model developed can capture the pressure sensitivity of the active layer, which has been observed in experiments.

1. Introduction

To meet the current and future energy requirements during the transition from fossil fuels to sustainable and renewable energy sources, innovative solutions for energy storage are required. In the electrification of the transport sector, lithium-ion batteries (LIB) are currently the primary choice of power storage as they provide high energy and power densities. These features should be paired with good cyclability and life span as replacing batteries is cumbersome and expensive. One limit to the life span of LIBs is loss of charge capacity. For optimizing the performance, numerical models are invaluable tools as they provide the possibility to extend experimental observations without requiring

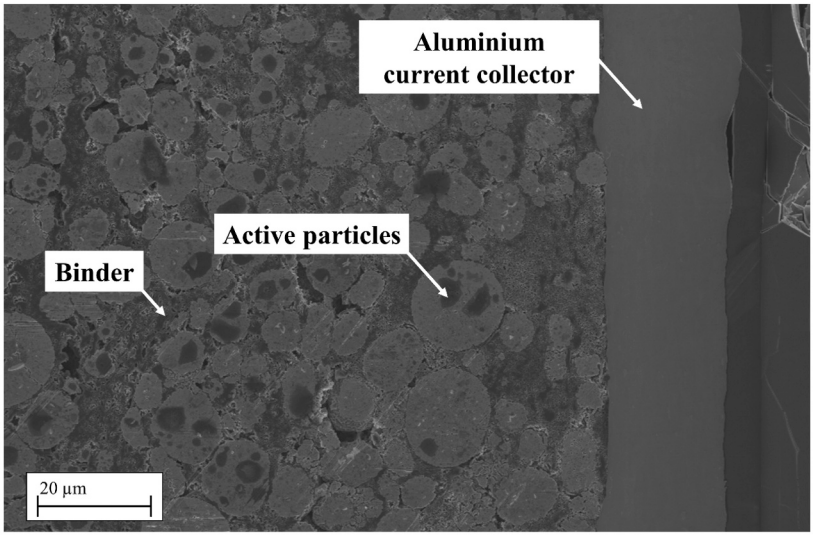
* Corresponding author.
E-mail address: erik.1.olsson@ltu.se (E. Olsson).

https://doi.org/10.1016/j.powtec.2023.118574
Received 17 January 2023; Received in revised form 29 March 2023; Accepted 17 April 2023
Available online 19 April 2023
0032-5910/© 2023 The Authors. Published by Elsevier B.V. This is an open access article under the CC BY license (http://creativecommons.org/licenses/by/4.0/).

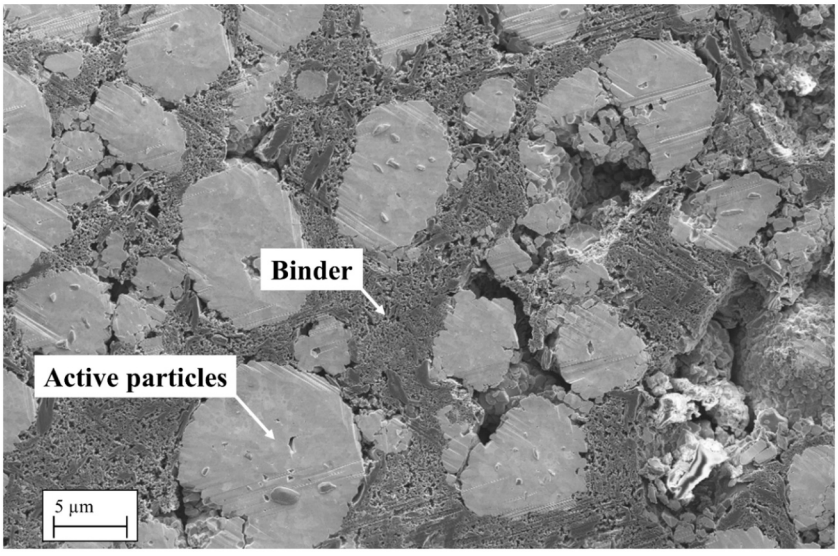
further experimental testing. They can also provide information on the local mechanical phenomenon in the structure which cannot be observed through experimental studies.

Lithium-ion batteries are built-up of thin positive and negative electrode layers, the cathode, and the anode. These layers consist of small electrochemically active particles bonded together with a binder material, composed of a polymer mixed with carbon additives, and several causes for the loss of charge capacity stems from mechanisms on the active particle scale. Capacity degradation of LIBs is a complex phenomenon with interacting electrical, chemical, and mechanical mechanisms. Mechanical loading, driven by the intercalation/deintercalation process, is one of the main causes for capacity loss in LIBs. During uptake of lithium-ions, the electrochemically active particles swell substantially. At subsequent release of lithium-ions the particles shrink to approximately their original size. This cyclic behaviour causes degradation both on the active particle level, in the form of cracking of the lithium storing particles, but also on the electrode level, as delamination of the active layer from the current collector and island formation in the electrode layer [1–4].

There is much evidence that the porosity and the bonding between the particles are important factors for the stability of charging-discharging cycles. For instance, the composition and behaviour of the binder have been shown to have a large influence. Hochgatterer et al. [5] suggested that the cohesive strength of the binder is an important factor. An increase of the binder strength led to an increased capacity retention [6]. Further evidence that the packing characteristics and contact between the particles are of importance is that a small external pressure on the battery cell is beneficial for the ageing. Cannarella and Arnold [7] showed that a small applied compressive stress (around 0.1 MPa) is beneficial for capacity retention. Larger pressures accelerate ageing. The interpretation is that pressure decreases the number of debonded particles due to swelling-shrinkage cycles but gives an increased risk of particle fracture. It is clear that important mechanisms for the capacity degradation stems from the granular microstructure of the battery electrodes. The granular microstructure can be seen in Fig. 1. One natural modelling approach for such materials, which will be



(a)



(b)

Fig. 1. Cross-sectional images of (a) a positive electrodes active layer and (b) the microstructure of the active layer. (Images taken by Dr. Fang Liu, Chalmers University of Technology, Gothenburg, Sweden.)

utilized in the present work, is the discrete element method (DEM), originally developed by Cundall and Strack [8], where the granular structure is modelled explicitly.

The manufacturing of the positive electrode also imposes mechanical loads, especially during the calendering process. When manufacturing electrodes, active particles are mixed with a polymeric binder material, carbon additives and solvents into a slurry. The slurry is then spread onto the current collector and dried. This is followed by calendering of the layer. The calendering process rearranges the microstructure of the active layer to decrease its porosity, and thus increasing its energy density. Calendering also improves the conductivity and adhesion in the electrode [9]. The calendering process has been studied extensively, both through experiments and simulations. Zheng et al. [10] studied the impact on mechanical and electrochemical properties from calendering on a positive electrode layer. They concluded from uniaxial tensile testing that calendering reduces the porosity in the electrode, leading to a mechanically stronger and stiffer network in tension. It also increases the conductivity between active particles in the electrode network. However, if too high calendering forces are used, the large amount of pore closure induced can negatively affect the electrochemical process between the electrode and the electrolyte. Meyer et al. [11] studied the impact of the calendering pressure and the calendering speed on the final electrode density and porosity. They could show that the relation of the final electrode density and the calendering line load followed an exponential behaviour. An experimental study was performed by Diener et al. [12], where the impact of the mass loading and the binder/particle ratio on the elastic and plastic deformation of the electrode layer was investigated. They demonstrated that an increased mass loading (i.e. a initially thicker electrode layer) and an increase of binder content decreased the elastic spring back during calendering. Sangrós Giménez et al. [13] developed a DEM simulation method to study the mechanical and microstructural properties of the electrode during the calendering process. The main conclusions were that the elastic recovery of the electrode height was dependent on the calendering pressure, by increasing the calendering pressure the elastic recovery decreased. Schreiner et al. [14–16] developed a methodology for simulating the calendering process of positive electrodes using DEM. The method relied on calibrating contact parameters in the DEM model, via a parametrization framework, to micromechanical indentation experiments on the electrode layer. After the contact models had been calibrated, the calendering phenomena is simulated for different mass loadings in the electrode layer and calendering gaps, where Schreiner et al. [16] could show that the electrode thickness after calendering matched between the simulations and the experiments. Primo et al. [17] performed an experimental study on the influence of the calendering parameters and the active layer material composition on the porosity of the electrode layer. They could show that the porosity of the electrode layer decreased when the ratio between binder and active particle mass was high. Further results also showed that when increasing the temperature of the calendering rolls, there was a greater porosity decrease for equivalent calendering pressures. During the assembly of the battery cell, the electrode layers can be either stacked, rolled or folded [9]. Rolling and folding also introduce mechanical stresses in both tension and compression in the electrode, which can lead to mechanical failure [18].

Various studies of the mechanical properties of the positive electrode have been performed, both experimentally and via simulations. For determining the properties of the individual domains in the active layer nanoindentation has been used excessively, both for the active particles and the binder [13,19–21]. The measurements of the active layers mechanical properties have proven to be more challenging as the active layer possesses a pressure sensitive behaviour, i.e. the mechanical properties in tension and compression differ. Nanoindentation has also been used on the active layer to determine the elastic and plastic properties of the active layer [14,22,23]. The tensile properties of the full electrode layer have been measured through tensile tests, and the active layer stiffness has been extracted from such measurements [22,24]. Zhu et al. [22] measured the elastic-plastic and fracture properties via nanoindentation. Tensile tests were also performed to measure the electrode force-displacement response coupled with in-situ scanning electron microscope observation to track the damage development in the active layer. The tensile force-displacement relations were then replicated using a 2D DEM model developed by Wang et al. [25]. Tensile tests of the positive electrode were also performed by Zhang et al. [24], and an estimation of the active layers stress-strain response was fitted to an isotropic linear hardening elastic-plastic model. Out-of-plane compression tests of the electrode was also performed and a stress-strain relation was fitted to the active layer's behaviour in compression. These constitutive models were then used in a finite element analysis of a blunt rod indentation test of multiple stacked electrode layers, which were compared to experiments. An experimental method for measuring the active layers in-plane mechanical properties was developed by Gupta et al. [26] and Üçel et al. [27]. U-shape bending of the electrode layer enables measurements of the in-plane stiffness both in compression and tension, while avoiding problems such as in-plane buckling, something which has not been performed in the literature before to the authors knowledge. The stiffness was measured both in tension and compression at various load rates which showed that the active layer material is both pressure and rate dependent. To the authors knowledge, no simulation model has been developed linking the mechanical behaviour of the active electrode layer to the contact properties of the binder domain and the active particles.

The scope of this article was to develop a framework for simulating the calendering process of a positive electrode layer, as well as the measurement of the layer's mechanical properties in tension and compression. The latter feature being the innovative and novel part of this work. The simulation framework consists of DEM contact models, both for the active particles and the binder, and the set up and assumptions of the simulations for the different processes. The framework developed was validated against the in-plane mechanical properties measured by Gupta et al. [26], in particular to show the difference in mechanical properties in tension and compression. This modelling framework provides an excellent foundation for further analysis of the mechanics in the electrode layer, such as swelling of the active particles from electrochemical loading.

This article initially presents an overview of DEM followed by the contact relations implemented for the binder domain and the active particles. It continues with the assumptions and setup of the simulation framework, including the creation of an uncalendered electrode layer, the calendering process and the mechanical loading in tension and compression. Finally, the results and conclusions are presented and discussed.

2. Discrete element method

The discrete element method, developed by Cundall and Strack [8], utilizes discrete points in space to represent spherical particles interacting through prescribed contact formulations. It uses an explicit time integration to determine the position of each particle through Newtons second law of motion. Using a Verlet type algorithm the position $\boldsymbol{X}_i(t)$, the velocity $\boldsymbol{V}_i(t)$ and the acceleration $\boldsymbol{a}_i(t)$, of each particle, are given by

$$\boldsymbol{a}_i(t) = \frac{\boldsymbol{F}_i(t)}{m_i}, \tag{1}$$

$$\boldsymbol{V}_i(t+\Delta t) = \boldsymbol{V}_i(t) + \boldsymbol{a}_i(t)\Delta t \tag{2}$$

$$\boldsymbol{X}_i(t+\Delta t) = \boldsymbol{X}_i(t) + \boldsymbol{V}_i(t)\Delta t \tag{3}$$

where t is the current time, Δt is the time increment, m_i is the mass of the particle and $\boldsymbol{F}_i(t)$ is the resulting force acting upon it. Pertinent expressions are used for integrating the rotational degrees of freedom. The resultant force on each particle consists of a sum of the tangential and

normal forces from all particles which it is in contact with, $\Sigma \boldsymbol{F}_i(t) = \Sigma \boldsymbol{F}_i^N(t) + \Sigma \boldsymbol{F}_i^T(t)$. Friction between particles was not considered, however tangential forces arise due to the binder contact formulation.

2.1. Stability of time integration

To ensure the computational stability of the explicit time integration, Cundall and Strack [8] proposed an estimate limit size of the time increment Δt to be

$$\Delta t = 2\sqrt{\frac{m_{min}}{k}}, \tag{4}$$

where m_{min} is the lowest mass of a particle and k is its largest contact stiffness. The time step used in simulations should be fractions smaller than this critical timestep to ensure stability in the time integration. If the loading is at quasi-static conditions, the limiting size of the timestep can be increased by applying mass scaling to the particle mass, thus reducing the total number of iterations, as shown by Thornton and Anthony [28]. For this application of DEM, the particles simulated interact with two different contact relations, contact between particles, and contact between particles with binder in between. These force relations will be presented below. Contact between particles and rigid walls is also possible, using the same contact conditions as for contact between two particles.

2.2. Macroscopic stress and force fabric tensor

DEM present local properties such as position and contact forces for the particles. As only global measures can be assessed during experiments, and not of individual contacts, a method to evaluate global stresses is required. Force fabric tensors and macroscopic stress tensors have been developed by several authors [28–30], building on the fabric tensor proposed by Satake [31] to evaluate contact distributions in granular media. Following Thornton and Anthony [28], the macroscopic stress tensor σ_{ij} is evaluated through

$$\sigma_{ij} = \frac{1}{V}\sum_{1}^{C} dNn_i n_j + \frac{1}{V}\sum_{1}^{C} dTn_i t_j, \tag{5}$$

where V is the volume of the system, C is the number of contacts, d is the distance between the particle centres, N is the normal contact force, T is the tangential contact force, n_i is the unit normal vector to the contact plane and t_i is the unit vector in the contact plane, parallel to the tangential contact force.

3. Contact models

The contact models determine the force between interacting particles. As mentioned above, two different contact formulations were utilized, one for the interaction between particles, from here on referenced

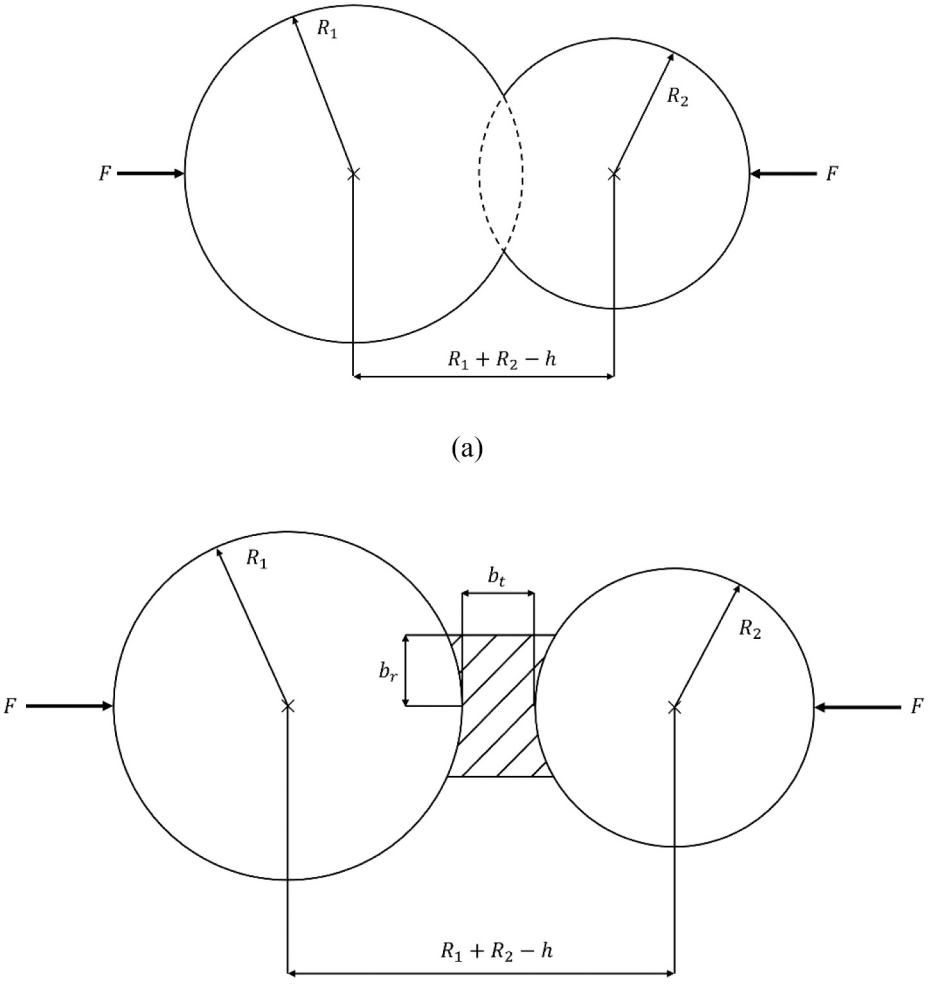


Fig. 2. Sketch of (a) the particle contact, (b) the binder contact.

to as particle contact, and one for the interaction between particles connected by binder, from here on referenced to as binder contact. Sketches of both contact types can be seen in Fig. 2.

3.1. Particle contact

The particle contact is assumed to have an elastic-plastic behaviour. The elastic particle contact is governed by the Hertzian contact model, which has been covered extensively in the literature [32]. The contact behaviour is given by

$$F = \frac{4}{3} E_{eff} \sqrt{R_{eff} h^3}, \tag{6}$$

where F is the normal contact force, E_{eff} is the effective Young's modulus, defined by

$$\frac{1}{E_{eff}} = \frac{1-\nu_1^2}{E_1} + \frac{1-\nu_2^2}{E_2}, \tag{7}$$

where E_i and ν_i are the two particles' Young's modulus and Poisson's ratio respectively. R_{eff} is the effective particle radius, defined by

$$\frac{1}{R_{eff}} = \frac{1}{R_1} + \frac{1}{R_2}, \tag{8}$$

where R_i is the radius of the two particles, and h is the overlap of the particles. This Hertz relation is valid for loading and unloading while the particles are in the elastic domain.

The particles deform elastically until the yield pressure is reached in the contact region. Sangrós Giménez et al. [13] suggested, based on an experimental study, a relation between the particle overlap where yielding occurs and the radius of a particle. The yield overlap h_y is dependent on the effective particle radius through a linear relation given by

$$h_y = k_y R_{eff}, \tag{9}$$

where $k_y = 8.6 \cdot 10^{-3}$ is the experimentally determined yield overlap coefficient and R_{eff} is the effective particle radius. The contact relation, during loading, in the plastic region is given by

$$F = F_y + 2E_{eff}\sqrt{R_{eff} h_y}\left(h - h_y\right), \tag{10}$$

where F_y is the contact force at yielding, given by Eq. (6) evaluated at $h = h_y$. This relation indicates that the force overlap relation is now linear, with a gradient given by the slope of the Hertz contact relation at the yield overlap. This contact relation is presented in detail in [13].

Unloading, after yielding has occurred in the particle, is done with the elastic Hertz relation given in Eq. (6). The plastic deformation, given by a plastic overlap h_{pl}, must now be considered during the elastic unloading. The plastic overlap is dependent on the elastic overlap required to give an elastic Hertz contact force of the same magnitude as the contact force at the maximum overlap. The plastic overlap is given by

$$h_{pl}\left(h_{max} > h_y\right) = h_{max} - \left(\frac{3h_{max}h_y^{\frac{1}{2}} - h_y^{\frac{3}{2}}}{2}\right)^{\frac{2}{3}}, \tag{11}$$

where h_{max} is the maximum overlap, larger than the yield overlap h_y. The shape of the force-overlap relation can be seen in Fig. 3. As stated above, frictionless contact was assumed which results in zero tangential contact force between the particles. This is motivated by the low influence of particle friction on the compaction stiffness shown by Olsson and Larsson in [33], particularly when compared to the shear stiffness of the binder domain.

It should be emphasized that the force-overlap relation in Fig. 3 is not completely compatible with a relation derived from classical frictionless contact mechanics. In short, this is due to the fact that only fully elastic and fully plastic contact is included in the relation. Accordingly, the elastic-plastic transition between these contact types, Johnson [34,35], is not accounted for. This is, however, most likely due to the fact that combined elastic-plastic effects are small and not detectable experimentally. This matter is not dwelled upon further and here, the experimentally determined relation is adhered to.

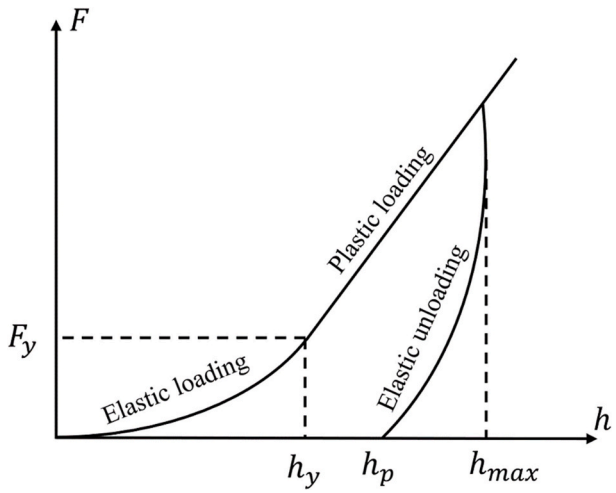


Fig. 3. Force – overlap relation for the particle contact where the elastic loading is given by Eq. (6), the plastic loading is given by Eq. (10), and the elastic unloading is given by Eq. (11).

3.2. Binder contact

The binder contact between two particles follows the assumptions proposed by Gudmundson and Larsson [36], where the binder is seen as a flat cylinder in loading between two flat surfaces. The cylinder is defined by its thickness b_t and its radius b_r. The binder material is assumed to be elastic-perfectly plastic and can take loads both in the normal and the tangential direction. The relation for the normal force F_n and the tangential force F_t is given by

$$F_n = \frac{(1-\nu)EA}{(1+\nu)(1-2\nu)} \frac{h + b_t}{b_t}, \tag{12}$$

$$F_t = \frac{EA}{2(1+\nu)} \frac{t}{b_t} \tag{13}$$

where E and ν is the Young's modulus and Poisson's ratio of the binder, A is the binders cross sectional area (following the binder radius b_r), b_t is the binder thickness, h is the particle overlap, initially negative as the binder is positioned between the particles, and t is the tangential displacement. The radius and thickness of the binder contact follows the radius of one of the particles in the contact, through a ratio between the binder thickness/radius and the particle radius. A fixed thickness ratio of $\frac{b_t}{R_i} = 0.5$ was used while the radius ratio, $\frac{b_r}{R_i}$, was varied in the study. The particle $i = 1, 2$ providing the input radius for the binder geometry is randomly selected in the contact pair.

Yielding in the binder is governed through evaluating the magnitude of the normal stress against the yield strength of the binder σ_y, (see-Fig. 4). The properties of the binder contact in the normal direction are valid both in tension and compression. Introducing damping was necessary in order to dissipate energy in the simulations. It was implemented as a viscoelastic model using a standard linear solid in Maxwell representation, with a ratio 0.75 between the relaxed and the instantaneous stiffness. The relaxation time in the Maxwell element was magnitudes shorter compared to the quasistatic loading time [37]. It should be noted that this viscoelastic model is only related to dampening of the system and not to capture the global viscoelastic effect of the electrode

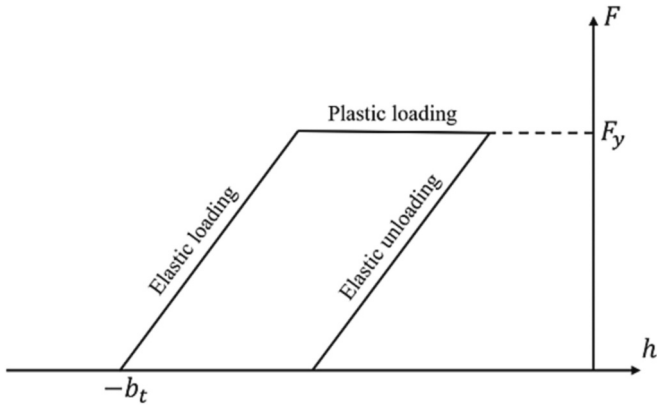


Fig. 4. Force-overlap relation for the binder contact.

layer. If a positive particle overlap is achieved for a binder contact, the binder and particle contact models contribute force to the contact in conjunction.

4. DEM analysis

The structure of a folded LIB cell can be seen in Fig. 5, and as stated earlier this study will focus on the positive electrode layer. The goal of the study was to model both the calendering and the mechanical measurement of the in-plane stiffness of the electrode layer using DEM. The DEM software utilized is an in-house code which previously has been used in other scientific articles, e.g. [38,39]. The DEM representation of the electrode layer utilized a representative volume element (RVE), which also can be seen in Fig. 5. The requirements to simulate these processes were methods to create an uncalendered electrode layer, calender the electrode layer, and applying the mechanical loading, all shown in Fig. 6. The specifications of the electrode layer, such as active layer thickness and active particle type, followed the commercial positive electrode used in [26] and the setup and assumptions of the simulation method will be presented below.

The computational requirement of DEM is determined by the number of simulated particles, the simulation time, and the minimum required integration time step. Simulating a full electrode layer, consisting of several million particles, would be unviable from a computational standpoint. Therefore, a RVE representation of the electrode was used. By applying periodic boundary conditions in the in-plane directions, forcing a particle exiting one side to re-enter on the opposite side, a quasi-infinite electrode layer could be represented. A convergence study was performed to determine the required size of the RVE to give homogenized and representative properties. The full simulation procedure, explained in detail below, was performed using the given geometry and material parameters presented, particularly using an elastic binder with a binder radius ratio of $\frac{b_r}{R} = 1.5$. The simulation was executed using 3000, 5000 and 10 000 discrete elements and it was concluded that 5000 elements, corresponding to an in-plane side length of 440 μm, was sufficient in the RVE while still utilizing a reasonable amount of computational resources.

The distribution of particle sizes was extracted from Ebner et al. [40], where X-Ray tomography was used to find the size distribution of NMC particles in a positive electrode layer. The particle diameter, in μm, followed a gamma distribution with the shape parameter $k = 4.9$ and the scale parameter $\theta = 2.6$. The particle diameters used were limited to $d = [8, 24]$ μm, this to limit the minimum time step, which is dependent on the mass of the smallest particle. This range captures 75% of the particle size distribution. Apart from this restriction the particle sizes followed a continuous distribution. The material properties for the particles and the binder domain can be found in Table 1. The material properties for the binder domain given are for the mixture of the polymer and the carbon additives. The type of contact between particles, i.e. particle or binder contact, at the contact initiation is randomly assigned, with a 60% probability of the contact being a binder contact. This ratio between binder and particle contacts was taken from DEM calculations on a comparable application [19].

4.1. Preparation of uncalendared electrode

In order to prepare the uncalendared electrode layer, a random loose packing method was utilized [42]. All particles were randomly generated in a block with predetermined side lengths, dependent on the expected final height of the electrode layer and the desired particle mass ratio in the active layer. The expected final calendering height of the layer was 111 μm, the mass ratio of active particles and the full active layer was $w_{NMC} = 0.86$ [26] and the density of the active layer was $\rho_{al} = 2230$ kgm^{-3}, given from the electrode manufacturer, CUSTOMCELLS. The initial height of the block was chosen to allow a distance between all particles at generation to form a binder contact, however bonding of the binder was not initiated during the packing. The particles were then allowed to naturally pack at the bottom of the box by gravity. When the

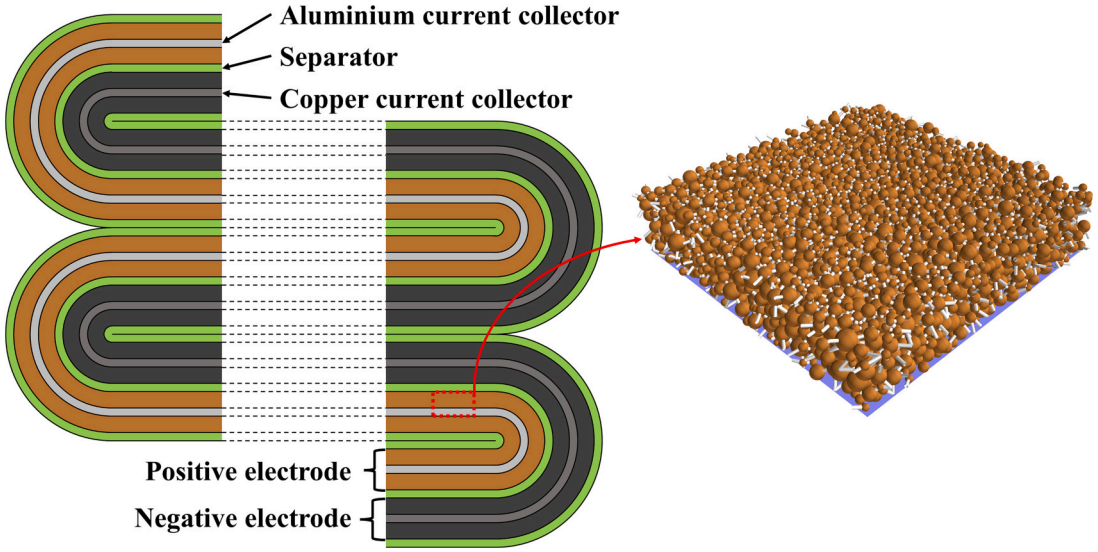


Fig. 5. Sketch of a folded battery cell and the RVE representation of the positive electrode.

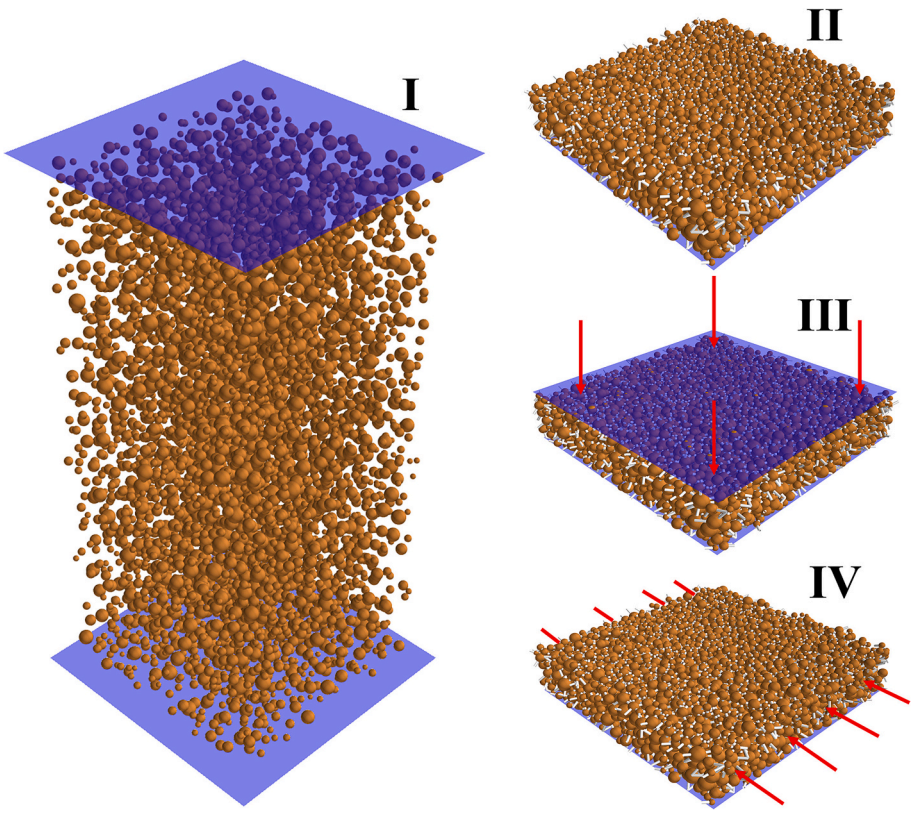


Fig. 6. The RVE of the positive electrode for the different steps in the simulation process: (I) random packing, (II) uncalendered electrode layer, (III) calendering process, (IV) in-plane mechanical loading.

Table 1
Material properties for the active particles and the binder.

Parameter	Material			
	Active particles (NMC)		Binder	
	Value	Reference	Value	Reference
Youngs Modulus [GPa]	140	[20,21]	2	[20]
Poisson's ratio [−]	0.3	[21] (Assumed)	0.3	[36]
Density [kgm^{-3}]	4630	[26] (Manufacturer)	–	–
Yield strength [MPa]	–	–	200	[41]
k_y[−]	8.59 10^{-3}	[13]	–	–

particles were at rest at the bottom, all particle velocities were set to zero before bonding in the binder contacts was activated, creating the final uncalendared electrode microstructure. As the packing is a dynamic process, mass scaling of the particles was not possible and thus not utilized in this simulation step.

4.2. Calendering

The mechanical aspects of the calendering process were considered during the setup of the calendering simulation. As the radius of the calendering rolls is magnitudes larger compared to the electrode thickness [11,12], the curvature of the calendering roll in the compression zone can be disregarded [13]. As both the current collector and the calendering roll have material stiffnesses magnitudes larger than the electrode layer, both the calendering roll and the current collector can be seen as rigid. The calendering roll and current collector is therefore modelled as rigid flat surfaces. It must however be noted that at large calendering pressures (>700 MPa), deformation of the current collector from the indentation of active particles can be present, something observed by Tran et al. [43]. During calendering, the calendering surface is displaced to a prescribed calendering height and is then removed until no remaining surface pressure is present. The calendering loading and unloading are performed in a quasi-static fashion, utilizing mass scaling of the particles. During the calendering process, the calendering pressure is measured through both the contact force on the calendering surface and the fabric stress tensor in the RVE. The validity of the calendering simulation is evaluated through the specific elastic spring back, as well as the pressure-displacement relation during the process. The specific elastic springback (*SES*) is given by

$$SES = \frac{h_1 - h_c}{h_0 - h_c}, \tag{14}$$

where h_0, h_c, h_1 is the active layer thickness before, during and after calendering, see Fig. 7. In the DEM model, the initial thickness h_0 and the residual thickness h_1 is measured when the calendering pressure is 0.5 MPa during the loading and unloading phase, this to diminish the impact of irregularities on the active layer surface. The minimum displacement height of the calendering surface for all calendering simulations was set to $h_c = 105$ μm.

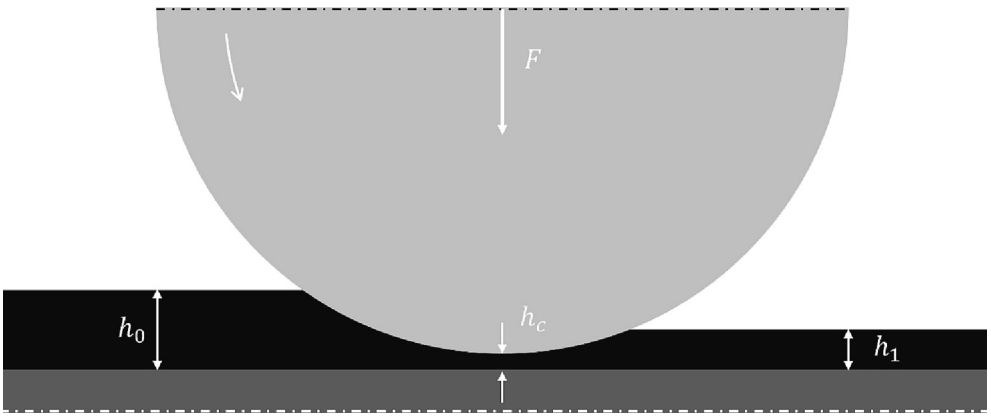


Fig. 7. Sketch of calendering process.

4.3. Determination of the mechanical properties

The in-plane mechanical loading was performed by tensile and compressive uniaxial loading through the periodic boundary conditions and the current collector. This represents in-plane tensile or compressive loading of the entire electrode layer. The unloading stiffness of the electrode layer was evaluated at different strain levels, both in compression and in tension. The unloading stiffness was determined by the slope of the macroscopic stress-strain curve at small unloading at the desired strain level. The strain levels for unloading, both in tension and compression, for all simulations were $\varepsilon = [0.25, 0.5, 1, 1.5, 2]\%$. These were compared to the unloading stiffnesses from the experiments performed by Gupta et al. [26], where the developed U-shape bending test had been utilized. The experimental setup placed the electrode layer between two face plates with a separation Δ, which would be decreased, and the face plate separation can be related to an average strain in the electrode layer. At certain face plate separations, small unloading's were made to measure the layers unloading stiffness. The experiments were performed at increasing face plate separation rates $\dot{\Delta}$, which corresponds to the displacement rate of the face plates. It should be noted that a constant face plate separation rate does not result in a constant in-plane strain rate, as the strain to face separation relation is not linear.

5. Results and discussions

Investigations have been performed considering the properties of the binder domain and the statistical accuracy of the model, following the random packing process. The results observed were the calendering pressure, the specific elastic springback for the calendering process, and the elastic unloading stiffness at mechanical loading at different strain levels. Initially the impact of the stiffness of the binder domain was investigated, this by using an elastic binder and increasing the binder radius ratio. This was followed by investigating the impact of plasticity in the binder domain. Finally, the statistical spread in the model was determined for two cases using an elastic binder with different binder radius.

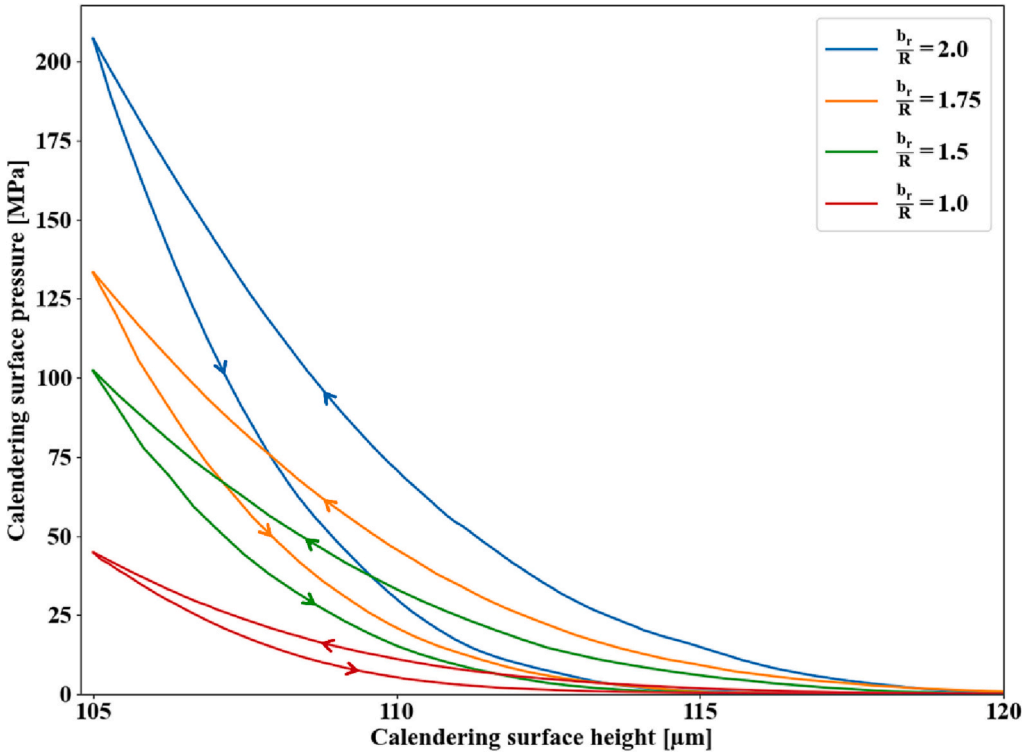


Fig. 8. Calendering surface pressure to surface height for four binder radius ratios.

Table 2
Specific elastic springback for different binder radius ratios.

Binder radius ratio	Specific elastic springback [%]
$\frac{b_r}{R} = 2.0$	74.3
$\frac{b_r}{R} = 1.75$	66.7
$\frac{b_r}{R} = 1.5$	72.7
$\frac{b_r}{R} = 1.0$	76.3

5.1. Impact of binder stiffness

The influence of the binder domain stiffness was investigated by performing the simulations with four ratios of the binder radius, $\frac{b_r}{R} = [1, 1.5, 1.75, 2]$, while assuming that the binder material is elastic. The calendering pressure can be seen in Fig. 8 and the specific elastic springback can be seen in Table 2. As the stiffness of the binder scales with the binder radius squared, the maximum calendering pressure scales linearly with the binder stiffness. At the same time, the specific elastic springback is reasonably constant, this as the binder is elastic and the only plastic deformation in the system arise in the particle contacts, the influence of plasticity in the binder domain is studied below. The unloading stiffness of the electrode layer, seen in Fig. 9, show that the range of binder stiffnesses used in the simulations captures the spread in the experimental unloading stiffness. The range of unloading stiffness for different load rates, seen in the experiments, is attributed to the viscoelastic behaviour of the binder material. This enables the model to capture the stiffness range given by the immediate and the relaxed stiffness of the electrode layer, following the viscoelastic properties of the binder domain. The simulation also captures the different unloading stiffness behaviours in compression and in tension. The trend of a constant unloading stiffness in tension at increasing strain levels and an increasing unloading stiffness in compression matches the trend observed in [26]. The constant unloading stiffness in tension for increasing strain levels is due to the fact that the load bearing capabilities in tension in the layer is only governed by the binder domain, as the non-adhesive particle contacts only take load in compression. On the contrary, the increasing unloading stiffness in compression with increasing compression strains is due to an increasing number of particle contacts with increasing strain levels, as can be seen in Fig. 10. Fig. 10 also indicate a similar number of particle contacts during the mechanical loading process for all binder radius ratios, apart from the most compliant binder with a radius ratio of $\frac{b_r}{R} = 0.10$. The case with the most compliant binder has initially (i.e. at zero strain) a higher number of particle contacts, however the trend of increasing number of particle contacts in compression is similar to the other cases. The initially higher number of particle contacts is due to the more compliant binder's inability to separate the particles to the same degree during the packing and calendering process.

5.2. Impact of plasticity in the binder

Following the investigation of the impact of the binder stiffness on the mechanical properties, the impact of plasticity in the binder domain was studied. A binder radius ratio of $\frac{b_r}{R} = 1.5$ was used to capture the lower bound of the experimental unloading stiffness, seen in Fig. 9. The calendering pressure, seen in Fig. 11, show that an elastic-plastic binder gives a lower calendering pressure compared to an elastic binder, which indicates that the binder domain deforms plastically during the calendering process. There is also a considerable decrease in the specific elastic springback, seen in Table 3, which indicated that more energy is dissipated in the system from the plastic deformation of the binder and particles. As for the unloading stiffness, the impact of plasticity did not have a significant impact, neither in tension nor compression as indicated in Fig. 12. This because the unloading is close to elastic, both for the particle contacts and the binder contacts. Further investigations of the layers mechanical properties will be performed in future studies, including e.g. cyclic mechanical loading, swelling of active particles from electrochemical loading and cracking of active particles.

5.3. Statistical spread in results

Finally, the statistical spread of the results determined numerically

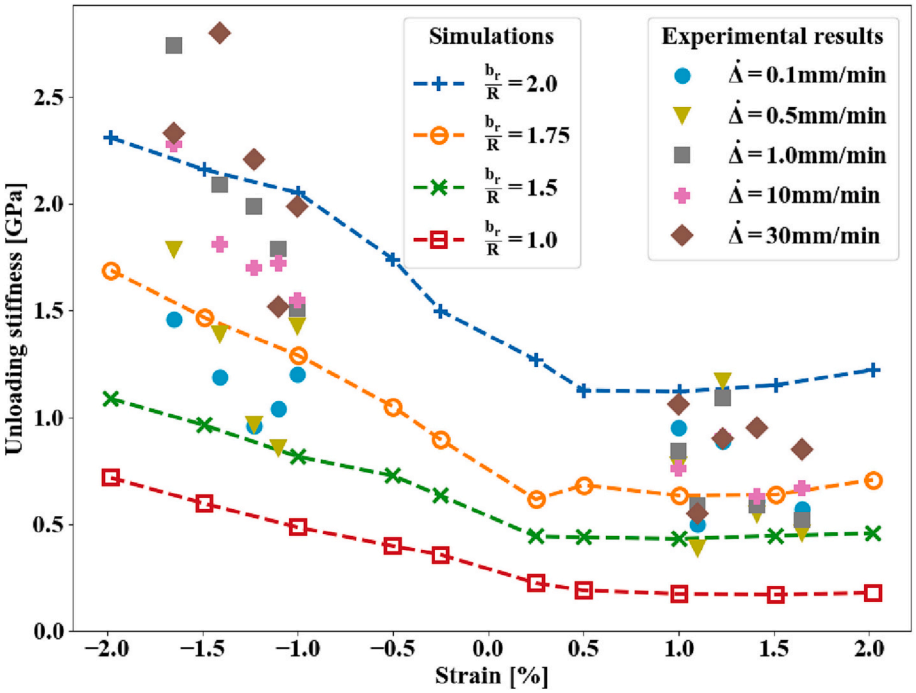


Fig. 9. Unloading stiffness for four binder radius ratios compared with the experimental results from [26].

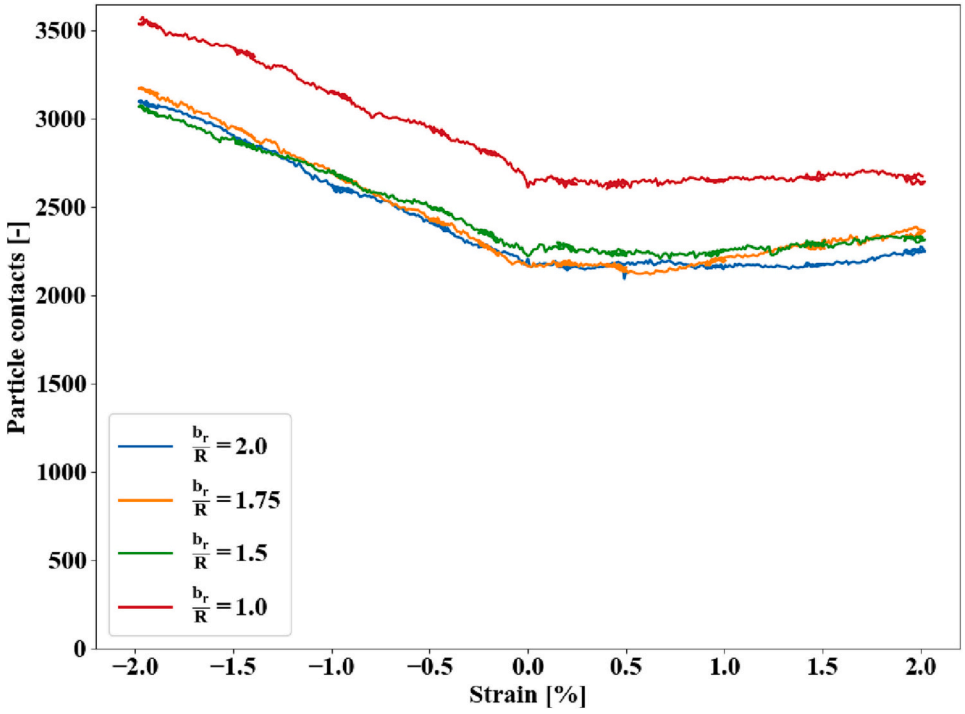


Fig. 10. Number of particle contacts during the mechanical loading for all simulated binder radius ratios.

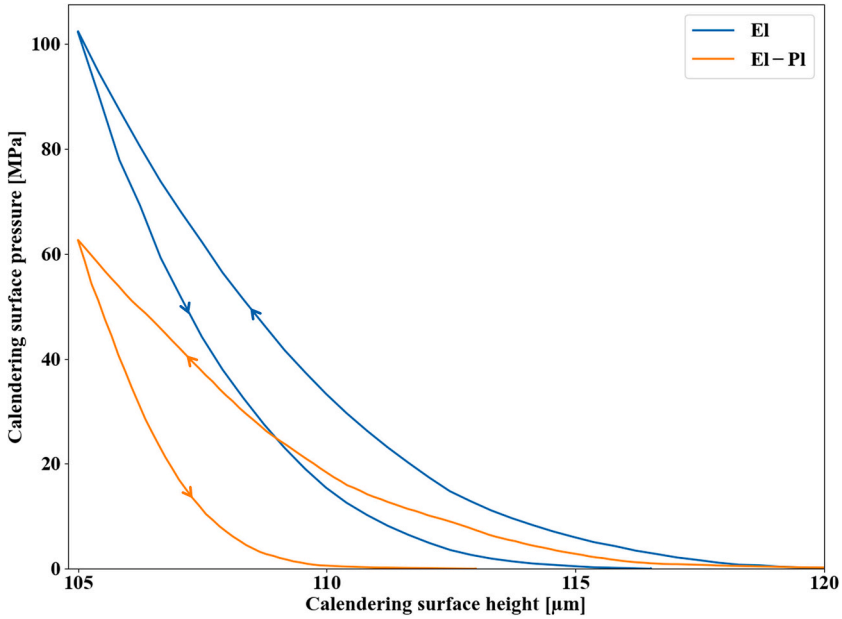


Fig. 11. Calendering pressure for the elastic and elastic-plastic binder.

Table 3
Specific elastic springback for the elastic and elastic-plastic binder.

Material model	Specific elastic springback [%]
El	72.7
El − Pl	39.8

was investigated. As the packing process is random in nature, the influence of the initial packing was investigated for two cases through five identical simulations. The simulations were run with an elastic binder material and a binder radius ratio of $\frac{b_r}{R} = [1.5, 2.0]$, this to capture the lower and upper bound of the experimental unloading stiffness. The calendering pressure can be seen in Fig. 13 and the unloading stiffnesses can be seen in Fig. 14. The mean and standard deviation of the specific elastic springback can be seen in Table 4. For the unloading stiffness, there is a larger spread in unloading stiffness at high compression strains compared to unloading stiffness in compression at low strain levels and unloading stiffness in tension. This could be explained by the fact that the unloading stiffness in compression is governed by the particle contacts, and thus also by the packing of particles.

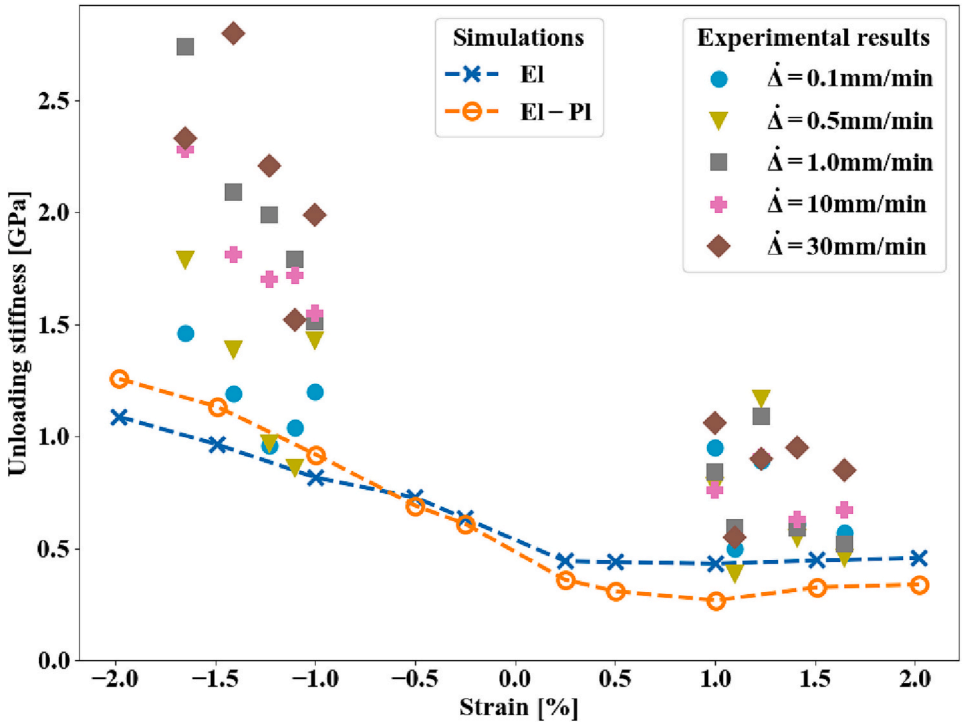


Fig. 12. Unloading stiffness for the elastic and elastic-plastic binder compared with the experimental results from [26].

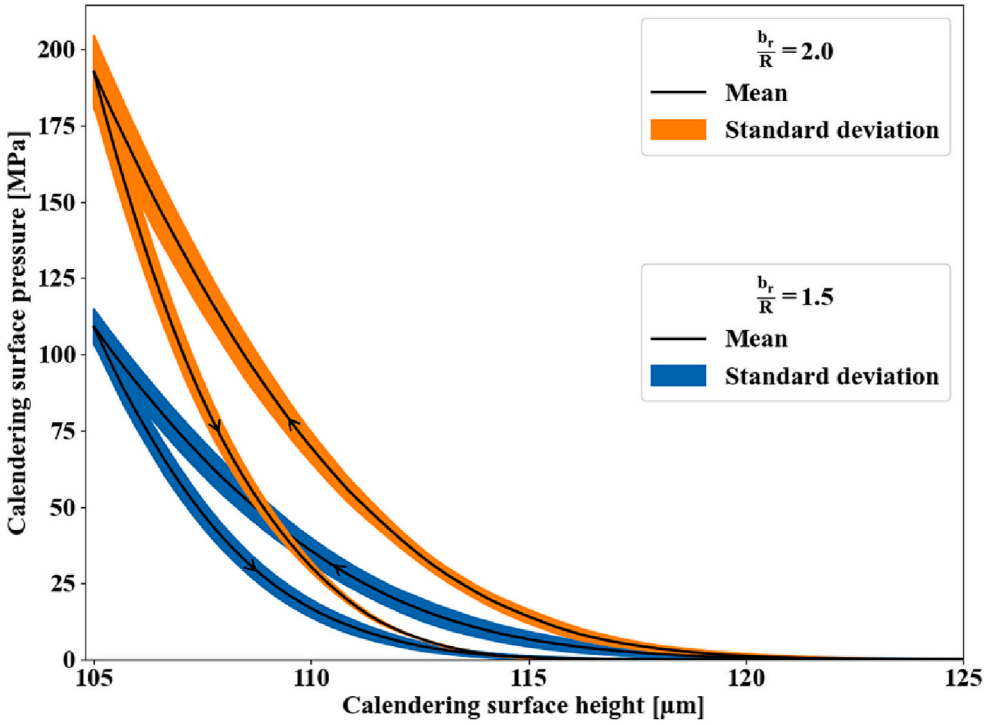


Fig. 13. Mean and standard deviation of the calendering pressure.

6. Conclusions

In this study, a DEM modelling framework was developed to investigate the mechanical behaviour of a positive electrode active layer of a lithium-ion battery. These were the main conclusions:

1. A methodology to simulate the creation of a uncalendered electrode, the calendering process and the measurement of in-plane unloading stiffness, both in tension and in compression, has been developed.
2. Both the mechanical properties of the binder domain and the active particles in contact govern the global mechanical behaviour of the active layer.

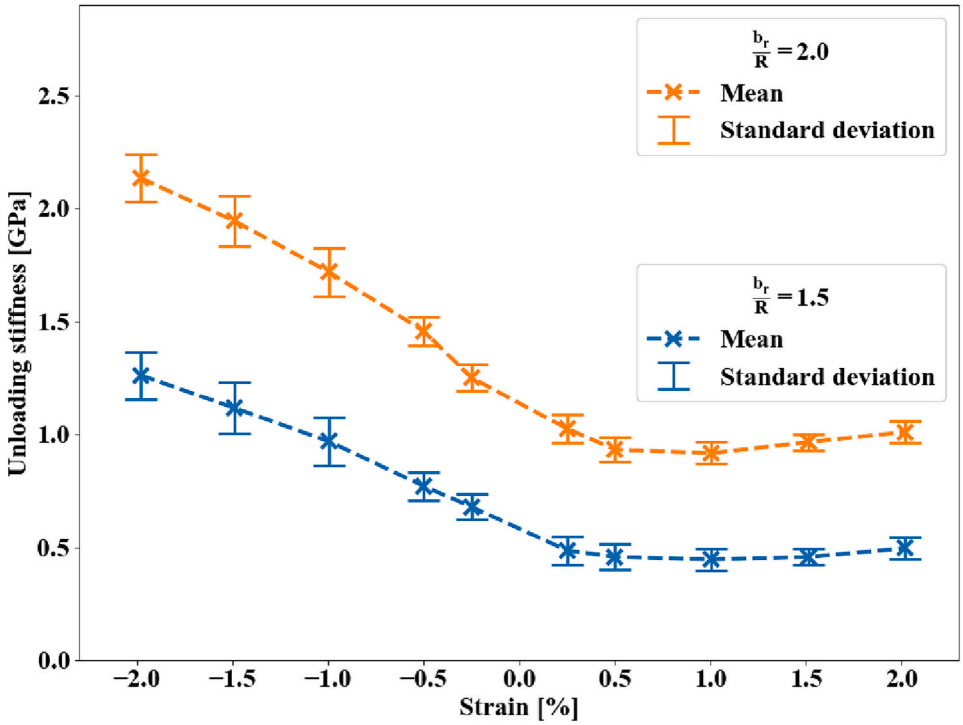


Fig. 14. Mean and standard deviation of the unloading stiffness.

Table 4
Mean and standard deviation of the specific elastic springback for two different binder radius ratios.

Binder radius ratio	Specific elastic springback [%]	
	Mean	Standard deviation
$\frac{b_r}{R} = 2.0$	64.7	8.26
$\frac{b_r}{R} = 1.5$	68.6	4.57

3. The model captures the experimentally observed rate-dependent unloading stiffness range of the electrode layer, which is caused by the viscoelastic binder.
4. The model captures the different unloading stiffness behaviours of the electrode layer in compression and in tension, as observed in experiments.

CRediT authorship contribution statement

Axel Lundkvist: Conceptualization, Methodology, Software, Formal analysis, Writing – original draft, Writing – review & editing. **Per-Lennart Larsson:** Conceptualization, Writing – original draft, Writing – review & editing, Supervision. **Erik Olsson:** Conceptualization, Software, Writing – original draft, Writing – review & editing, Supervision, Funding acquisition.

Declaration of Competing Interest

The authors declare that they have no known competing financial interests or personal relationships that could have appeared to influence the work reported in this paper.

Data availability

The code is shared on github https://github.com/axlun/DEMsim.

Acknowledgements

The authors want to acknowledge M.Sc. Elaheh Etemadi for important contributions to the simulation methodology, Prof. Peter Gudmundson for helpful discussions, and Energimyndingheten (the Swedish Energy Agency) for financing the project through the grant 46558-1.

References

[1] W.J. Zhang, A review of the electrochemical performance of alloy anodes for lithium-ion batteries, J. Power Sources 196 (1) (2011) 13–24, https://doi.org/10.1016/j.jpowsour.2010.07.020.
[2] A. Mukhopadhyay, B.W. Sheldon, Deformation and stress in electrode materials for Li-ion batteries, Prog. Mater. Sci. 63 (January) (2014) 58–116, https://doi.org/10.1016/j.pmatsci.2014.02.001.
[3] J. Vetter, et al., Ageing mechanisms in lithium-ion batteries, J. Power Sources 147 (1–2) (2005) 269–281, https://doi.org/10.1016/j.jpowsour.2005.01.006.
[4] J. Zhu, T. Wierzbicki, W. Li, A review of safety-focused mechanical modeling of commercial lithium-ion batteries, J. Power Sources 378 (November) (2018) 153–168, https://doi.org/10.1016/j.jpowsour.2017.12.034.
[5] N.S. Hochgatterer, et al., Silicon/graphite composite electrodes for high-capacity anodes: influence of binder chemistry on cycling stability, Electrochem. Solid-State Lett. 11 (5) (2008) 1–6, https://doi.org/10.1149/1.2888173.
[6] L. Chen, X. Xie, J. Xie, K. Wang, J. Yang, Binder effect on cycling performance of silicon/carbon composite anodes for lithium ion batteries, J. Appl. Electrochem. 36 (10) (2006) 1099–1104, https://doi.org/10.1007/s10800-006-9191-2.
[7] J. Cannarella, C.B. Arnold, Stress evolution and capacity fade in constrained lithium-ion pouch cells, J. Power Sources 245 (2014) 745–751, https://doi.org/10.1016/j.jpowsour.2013.06.165.
[8] P.A. Cundall, O.D.L. Strack, A discrete numerical model for granular assemblies, Geeotechnique 29 (29) (1979) 47–65.
[9] A. Kwade, W. Haselrieder, R. Leithoff, A. Modlinger, F. Dietrich, K. Droeder, Current status and challenges for automotive battery production technologies, Nat. Energy 3 (4) (2018) 290–300, https://doi.org/10.1038/s41560-018-0130-3.
[10] H. Zheng, L. Tan, G. Liu, X. Song, V.S. Battaglia, Calendering effects on the physical and electrochemical properties of Li[Ni 1/3Mn 1/3Co 1/3]O 2 cathode, J. Power Sources 208 (2012) 52–57, https://doi.org/10.1016/j.jpowsour.2012.02.001.
[11] C. Meyer, H. Bockholt, W. Haselrieder, A. Kwade, Characterization of the calendering process for compaction of electrodes for lithium-ion batteries, J. Mater. Process. Technol. 249 (November) (2017) 172–178, https://doi.org/10.1016/j.jmatprotec.2017.05.031.
[12] A. Diener, S. Ivanov, W. Haselrieder, A. Kwade, Evaluation of deformation behavior and fast elastic recovery of lithium-ion battery cathodes via direct roll-gap detection during calendering, Energy Technol. 10 (4) (2022), https://doi.org/10.1002/ente.202101033.

[13] C. Sangrós Giménez, B. Finke, C. Schilde, L. Froböse, A. Kwade, Numerical simulation of the behavior of lithium-ion battery electrodes during the calendaring process via the discrete element method, Powder Technol. 349 (2019) 1–11, https://doi.org/10.1016/j.powtec.2019.03.020.
[14] D. Schreiner, A. Klinger, G. Reinhart, Modeling of the calendering process for lithium-ion batteries with DEM simulation, Proc. CIRP 93 (2020) 149–155, https://doi.org/10.1016/j.procir.2020.05.158.
[15] D. Schreiner, J. Lindenblatt, F.J. Günter, G. Reinhart, DEM simulations of the Calendering process: parameterization of the electrode material of Lithium-ion batteries, Proc. CIRP 104 (2021) 91–97, https://doi.org/10.1016/j.procir.2021.11.016.
[16] D. Schreiner, J. Lindenblatt, R. Daub, G. Reinhart, Simulation of the Calendering process of NMC-622 cathodes for lithium-ion batteries, Energy Technol. (2022), https://doi.org/10.1002/ente.202200442.
[17] E.N. Primo, M. Chouchane, M. Touzin, P. Vazquez, A.A. Franco, Understanding the calendering processability of Li(Ni0.33Mn0.33Co0.33)O2-based cathodes, J. Power Sources 488 (2021), 229361, https://doi.org/10.1016/j.jpowsour.2020.229361.
[18] A. Schilling, J. Schmitt, F. Dietrich, K. Dröder, Analyzing bending stresses on lithium-ion battery cathodes induced by the assembly process, Energy Technol. 4 (12) (2016) 1502–1508, https://doi.org/10.1002/ente.201600131.
[19] C. Sangrós Giménez, C. Schilde, L. Froböse, S. Ivanov, A. Kwade, Mechanical, electrical, and ionic behavior of lithium-ion battery electrodes via discrete element method simulations, Energy Technol. 8 (2) (2020) 1–10, https://doi.org/10.1002/ente.201900180.
[20] L.S. de Vasconcelos, R. Xu, J. Li, K. Zhao, Grid indentation analysis of mechanical properties of composite electrodes in Li-ion batteries, Extrem. Mech. Lett. 9 (2016) 495–502, https://doi.org/10.1016/j.eml.2016.03.002.
[21] R. Xu, H. Sun, L.S. de Vasconcelos, K. Zhao, Mechanical and structural degradation of LiNi x Mn y co z O 2 cathode in Li-ion batteries: an experimental study, J. Electrochem. Soc. 164 (13) (2017) A3333–A3341, https://doi.org/10.1149/2.1751713jes.
[22] J. Zhu, X. Zhang, H. Luo, E. Sahraei, Investigation of the deformation mechanisms of lithium-ion battery components using in-situ micro tests, Appl. Energy 224 (2018) 251–266, https://doi.org/10.1016/j.apenergy.2018.05.007.
[23] C. Sangrós, B. Finke, C. Nowak, C. Schilde, A. Kwade, Structural and mechanical characterization of lithium-ion battery electrodes via DEM simulations 29, 2018, pp. 2312–2321, https://doi.org/10.1016/j.apt.2018.05.014.
[24] C. Zhang, J. Xu, L. Cao, Z. Wu, S. Santhanagopalan, Constitutive behavior and progressive mechanical failure of electrodes in lithium-ion batteries, J. Power Sources 357 (2017) 126–137, https://doi.org/10.1016/j.jpowsour.2017.04.103.
[25] Z. Wang, L. Yang, S. Zhu, W.L. Song, H. Sen Chen, Exploring mechanical failure of porous electrode meso structure using the discrete element method, Extrem. Mech. Lett. 46 (2021), 101252, https://doi.org/10.1016/j.eml.2021.101252.
[26] P. Gupta, I.B. Üçel, P. Gudmundson, E. Olsson, Characterization of the constitutive behavior of a cathode active layer in lithium-ion batteries using a bending test method, Exp. Mech. 60 (6) (2020) 847–860, https://doi.org/10.1007/s11340-020-00613-5.
[27] B. Üçel, P. Gupta, P. Gudmundson, Experimental determination of the constitutive properties of a graphite anode layer in lithium-ion batteries using a bending test method, J. Energy Storage 46 (February) (2022) 103845, https://doi.org/10.1016/j.est.2021.103845.
[28] C. Thornton, S.J. Anthony, Quasi-static deformation of particulate media, Phil. Trans. R. Soc. Lond. A 356 (1998) 2763–2782.
[29] J. Christoffersen, M.M. Mehrabadi, S. Nemat-Nasser, A micromechanical description of granular material behavior, J. Appl. Mech. Trans. ASME 48 (2) (1981) 339–344, https://doi.org/10.1115/1.3157619.
[30] L. Rothenburg, A.P.S. Selvadurai, A micromeehanical definition of the Cauchy stress tensor for particulate media, in: Mechanics of Structured Media: Proceedings of the International Symposium on the Mechanical Behaviour of Structured Media, 1981, pp. 469–486.
[31] M. Satake, Fabric tensor in granular materials, in: Deformation and Failure of Granular Materials. IUTAM Symposium, Delft, 1982, pp. 63–68.
[32] H. Hertz, Ueber die Berührung fester elastischer Körper, J. Reine Angew. Math. 1882 (92) (1882) 156–171, https://doi.org/10.1515/crll.1882.92.156.
[33] E. Olsson, P.L. Larsson, On the effect of particle size distribution in cold powder compaction, J. Appl. Mech. Trans. ASME 79 (5) (2012), https://doi.org/10.1115/1.4006382.
[34] K.L. Johnson, The correlation of indentation experiments, J. Mech. Phys. Solids 18 (2) (1970) 115–126, https://doi.org/10.1016/0022-5096(70)90029-3.
[35] K.L. Johnson, Contact Mechanics, Cambridge University Press, Cambridge, 1989.
[36] P. Gudmundson, P.L. Larsson, An analytic model for effective mechanical properties and local contact stresses in lithium-ion porous electrodes, Extrem. Mech. Lett. 42 (2021), 101067, https://doi.org/10.1016/j.eml.2020.101067.
[37] E. Olsson, D. Jelagin, A contact model for the normal force between viscoelastic particles in discrete element simulations, Powder Technol. 342 (2019) 985–991, https://doi.org/10.1016/j.powtec.2018.10.022.
[38] D. Jelagin, E. Olsson, C. Raab, M.N. Partl, Experimental and numerical modelling of shear bonding between asphalt layers, Road Mater. Pavem. Des. (2023), https://doi.org/10.1080/14680629.2023.2180298.
[39] E. Olsson, D. Jelagin, M.N. Partl, Numerical evaluation of crushing resistance of unbound road material, in: Proceedings of the 9th International Conference on Maintenance and Rehabilitation of Pavements—Mairepav 9, 2020, pp. 201–210.
[40] M. Ebner, F. Geldmacher, F. Marone, M. Stampanoni, V. Wood, X-ray tomography of porous, transition metal oxide based lithium ion battery electrodes, Adv. Energy Mater. 3 (7) (2013) 845–850, https://doi.org/10.1002/aenm.201200932.
[41] A.H.S. Iyer, P. Gupta, P. Gudmundson, A. Kulachenko, Measuring Microscale Mechanical Properties of PVdF Binder Phase Using Micromechanical Testing, Manuscript to be submitted for international publication, 2023.
[42] H. Tangri, Y. Guo, J.S. Curtis, Packing of cylindrical particles: DEM simulations and experimental measurements, Powder Technol. 317 (2017) 72–82, https://doi.org/10.1016/j.powtec.2017.03.058.
[43] H.Y. Tran, G. Greco, C. Täubert, M. Wohlfahrt-Mehrens, W. Haselrieder, A. Kwade, Influence of electrode preparation on the electrochemical performance of LiNi 0.8Co 0.15Al 0.05O 2 composite electrodes for lithium-ion batteries, J. Power Sources 210 (2012) 276–285, https://doi.org/10.1016/j.jpowsour.2012.03.017.